

Supporting Information For

**A highly conducting organic metal derived from an organic-transistor material:
benzothienobenzothiophene**

Tomofumi Kadoya,^{*,^a} Minoru Ashizawa,^a Toshiki Higashino,^a Tadashi Kawamoto,^a
Shohei Kumeta,^a Hidetoshi Matsumoto,^a and Takehiko Mori^{a,b}

^aDepartment of Organic and Polymeric Materials, Tokyo Institute of Technology,
O-okayama 2-12-1, Tokyo 152-8552, Japan

^bACT-C, JST, Honcho, Kawaguchi, 332-0012, Japan

E-mail: kadoya.t.aa@m.titech.ac.jp

Contents

1. Redox potentials and the Fermi energy
2. Crystal structure
3. Calculation of energy bands, Fermi surface, and HOMO
4. Electrical conductivity measurement and estimation of drift mobility
5. Arrhenius plots
6. Relaxation of the resistivity
7. Resistivity under physical pressure
8. ESR measurements

1. Redox potentials and the Fermi energy

Cyclic voltammograms (CVs) were measured in dichloromethane containing tetrabutylammonium hexafluorophosphate as a supporting electrolyte at a scan speed of 0.1 V/s. Counter and working electrodes were made of Pt and glassy carbon, respectively, and the reference electrode was Ag/AgCl. The potentials were calibrated with the standard ferrocene/ferrocenium redox couple. As shown in Fig. S1, the onset potential (E^{onset}) of BTBT is 0.9 V corresponding to the HOMO level of 5.65 eV.¹ For other organic materials, the energy levels are estimated from the redox potentials vs. SCE by adding 4.44 eV.^{S1}

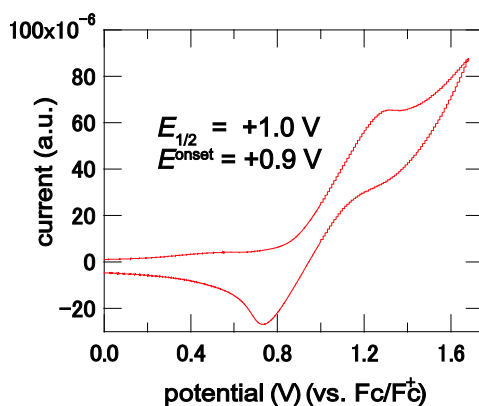


Fig. S1 Cyclic voltammogram of BTBT.

2. Crystal structure

The X-ray diffraction data of the PF₆ salt were collected by using a Rigaku AFC-7R diffractometer with graphite monochromated Mo K α radiation (0.71069 Å). The crystal data are listed in Table S1. The crystal structures were solved by the direct method (SIR2008^{S2}) and refined by full-matrix least squares on F^2 (SHELXL-97^{S3}). The optical image of the crystals, the temperature dependence of the lattice constants and X-ray photograph are depicted in Fig. S2. X-ray photograph were taken on a Rigaku R-AXIS RAPID-II diffractometer using CuK α radiation ($\lambda = 1.54187\text{ \AA}$) monochromated by confocal mirror (Rigaku VariMax).

To clarify the origin of the resistivity jump, low-temperature X-ray crystal structure analysis is carried out. All lattice constants are perfectly continuous at around 150 K (Fig. S2(b)). At 110 K, no extra spots or diffusive lines are detected (Fig. S2(c)), and the crystal structure is analyzed under the same tetragonal space group $P-42_1c$ (no. 114).

An attempt to analyze the low-temperature structure under the reduced symmetry (*P*-4) has not improved the result. Accordingly, the structural change associated with the resistivity jump is, if any, small.

Table S1. Crystallographic data of (BTBT)₂PF₆ at 298 K and 100 K

formula	C ₂₈ H ₁₆ S ₄ PF ₆	C ₂₈ H ₁₆ S ₄ PF ₆
crystal size	0.12 × 0.12 × 0.25 mm ³	0.12 × 0.12 × 0.25 mm ³
<i>T</i> (K)	298	100
crystal system	tetragonal	tetragonal
space group	<i>P</i> -42 ₁ c	<i>P</i> -42 ₁ c
<i>a</i> (Å)	13.490(2)	13.407(5)
<i>c</i> (Å)	6.734(2)	6.638(6)
<i>V</i> (Å ³)	1225.4(4)	1193(2)
<i>Z</i>	2	2
<i>D</i> _{calc} (g cm ⁻³)	1.695	1.741
independent reflections	1120	1065
observed reflections [<i>I</i> > 2σ(<i>I</i>)]	718	863
<i>R</i> 1; <i>wR</i> 2 [<i>I</i> > 2σ(<i>I</i>)]	0.0392; 0.1368	0.0438; 0.1291
GOF	0.854	0.951

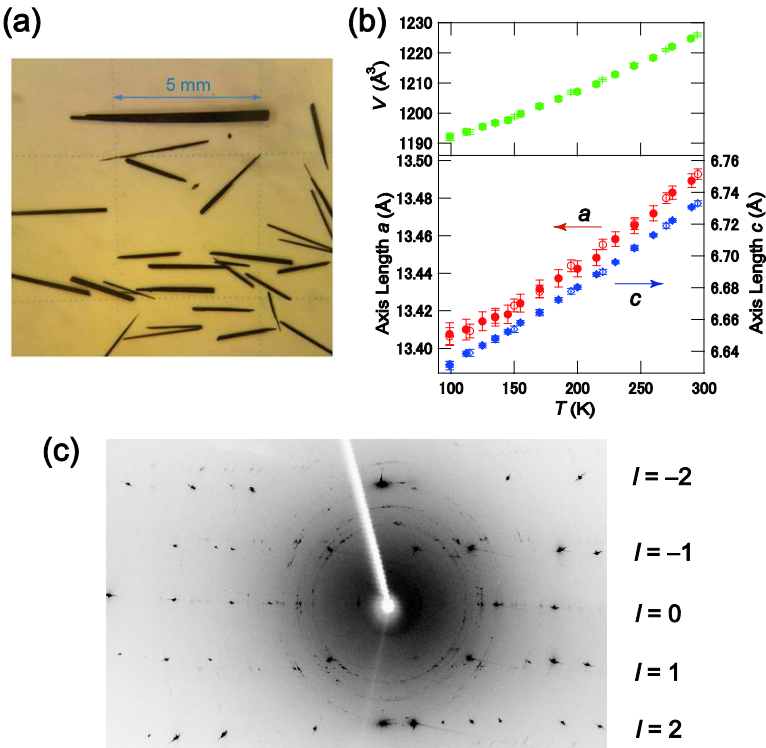


Fig. S2 (a) Optical images of single crystals of $(\text{BTBT})_2\text{PF}_6$ and (b) temperature dependence of the lattice constants a (red circles), c (blue diamonds) and V (green circles). Closed symbols are from the cooling run, and the open symbols are from the heating run. (c) X-ray photograph of $(\text{BTBT})_2\text{PF}_6$ at 110 K.

3. Calculation of energy bands, Fermi surface, and HOMO

The energy bands and the Fermi surface were calculated on the basis of the tight-binding approximation with the intermolecular overlap integrals of HOMO obtained from the MOPAC, AM1 molecular orbital calculation.^{S4} As shown in Fig. S3, the HOMO population is largely located on the sulfur atoms, and large intermolecular interaction is expected to form a efficient carrier path along the c axis. The calculated transfer integrals are listed in the caption of Fig. 1.

Fig. S4 shows the band structure and the Fermi surface. The bandwidth is comparatively small (~ 0.35 eV) owing to the relatively small transfer integral between the stacked molecules (Fig. 1). The open Fermi surface is characteristic of the one-dimensional band.

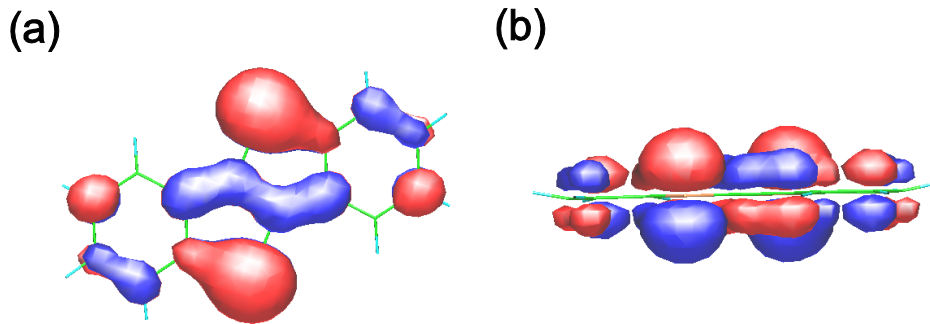


Fig. S3 HOMO of BTBT molecule calculated by MOPAC, (a) viewed perpendicular to, and (b) parallel to the molecular plane.

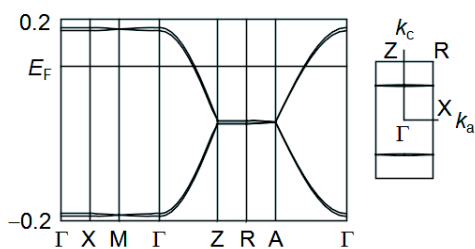


Fig. S4 Energy band structure and the Fermi surface of $(\text{BTBT})_2\text{PF}_6$. M: $(\pi/a, \pi/a, 0)$, R: $(0, \pi/a, \pi/c)$, and A: $(\pi/a, \pi/a, \pi/c)$.

4. Electrical conductivity measurement and estimation of drift mobility

Electrical resistivities were measured by the conventional four-probe method using low-frequency AC current. Gold wires ($15 \mu\text{m}$ ϕ diameter) were attached to a crystal using carbon paste. Measurements were carried out parallel and perpendicular to the conducting c -axis. A pressure cell of the clamp type was used with an oil Daphne #7373 as a pressure medium. The pressure was estimated from the resistance change of a manganin wire at room temperature.

Drift mobility μ is evaluated from the following equation,

$$\mu = \frac{\sigma}{ne}$$

where σ is the electrical conductivity, n is the carrier number in a unit cell, and e is the elementary charge.

$(\text{BTBT})_2\text{PF}_6$ has the 2:1 composition, so one BTBT molecule has 0.5+ charge because PF_6^- has 1- charge. According to Fig. 1(a), a unit cell includes four BTBT molecules. From these, the drift mobility at room temperature is,

$$\begin{aligned}\mu &= \frac{\sigma}{ne} \\ &= \frac{1500 \text{ S/cm}}{4 \times 0.5 \times \frac{1}{1225 \times 10^{-24} \text{ cm}^3} \times (1.6 \times 10^{-19} \text{ C})} \\ &= 5.7 \text{ cm}^2/\text{Vs}\end{aligned}$$

5. Arrhenius plots

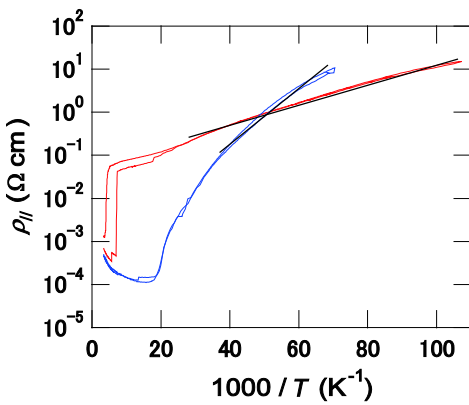


Fig. S5 Arrhenius plots of $(\text{BTBT})_2\text{PF}_6$. Red curve presents the result for a free sample, and the blue curve shows the result for an Apiezon coated sample.

Activation energy E_a was calculated from the equation,

$$\rho = \rho_0 \exp\left(\frac{E_a}{k_B T}\right)$$

where ρ is the resistivity, ρ_0 is a constant, k_B is the Boltzmann constant, and T is the temperature. From the straight part of the red curve in Fig. S5 E_a / k_B is obtained to be 57 K, and E_a is 4.8 meV. From the blue curve, E_a / k_B is similarly obtained to be 140 K, and E_a is 12 meV.

6. Relaxation of the resistivity

When the resistivity is measured again immediately after the first temperature cycle, the resistivity increases gradually from much higher temperatures as shown in Fig.

S6(a). However, when the resistivity is measured one month after the first measurement, the resistivity jumps approximately at the same temperature as the first measurement (Fig. S6(b)). The present observation suggests that after the largely hysteretic resistivity jump, the relaxation occurs during several weeks.

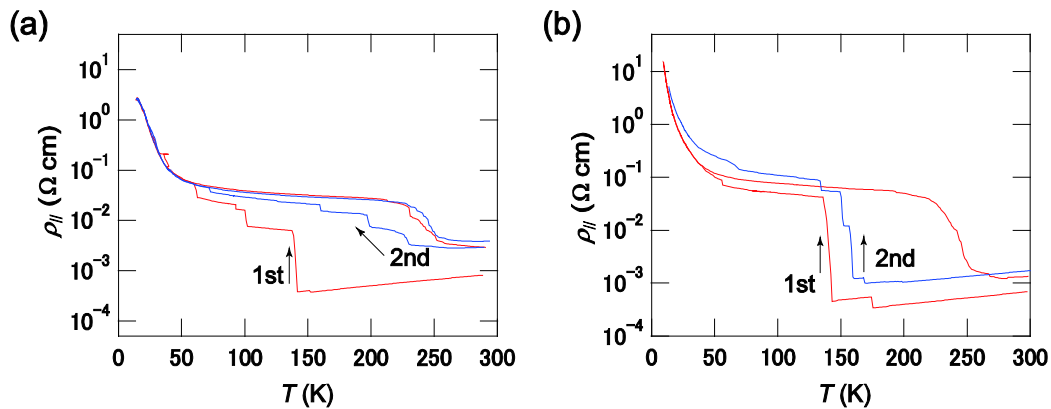


Fig. S6 Temperature dependence of the resistivity, (a) immediately after and (b) one month after the first measurement.

7. Resistivity under pressure

Fig. S7(a) shows pressure dependence of the resistivity measured using a clamp cell. The resistivity jumps around 1 kbar at room temperature, where the resistivity increases by one to two orders. This pressure-induced resistivity jump looks like the temperature-induced resistivity jump at 150 K. When reducing the pressure, the resistivity decreases gradually but does not entirely return to the original value. We can repeat the jump and recovery of the resistivity. After the first resistivity jump, the resistivity jump tends to occur at lower pressures. The pressure-induced insulating state reminds us $\text{Cu}(\text{DMDCNQI})_2$ (DMDCNQI: dimethyldicyanoquinonediimine),⁵⁵ where the Jahn-Teller distortion around Cu is the origin of the insulating state.

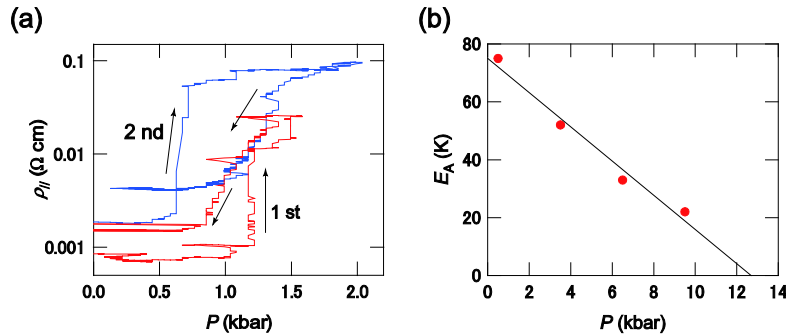


Fig. S7 (a) Pressure dependence of the resistivity at room temperature. The red curve is the first measurement, and the blue curve is the second measurement. (b) Activation energy plotted as a function of the low-temperature pressure. The low-temperature pressure values are reduced by 3 kbar from the room-temperature values.

8. ESR measurements

The ESR measurements were carried out for single crystals by using an X-band spectrometer (JEOL JES-TE100). The g values were calibrated by the spectra of diphenyl-(2,4,6-trinitrophenyl)iminoazanium (DPPH): $g = 2.0036$, and Li(TCNQ): $g = 2.0026$. Since the signal of the present sample was very close to DPPH and Li(TCNQ), the signal was not measured at the same time. Calibration was performed as follows. First, the g value of the sample was measured without DPPH and Li(TCNQ). Second, the g values of DPPH or Li(TCNQ) were measured under nearly the same conditions, and the differences of the g values from the reported values were evaluated. Finally, the sample g value was corrected on the basis of the evaluated difference. The corrected g values coincided with each other up to four digits for DPPH and Li(TCNQ).

The linewidth and the g values of a Dysonian signal were defined as shown in Fig. S8(a). The A and B values were directly estimated from the lineshape. Angle dependence of these parameters for the sample rotation around the a axis at room temperature was depicted in Fig. S8(b). From this, the g values were obtained to be $g_{\parallel c} = 2.002$ and $g_{\perp c} = 2.003$. Owing to the perpendicular molecular arrangement in the crystal, we could not directly relate these values to the g values of the molecule.

When the sample was rotated around the c axis, the signal was a perfect Lorentzian ($A / B \sim 1$), and the g value did not change (2.003) reflecting the tetragonal symmetry (Fig. S9).

For $H \parallel c$, the lineshape depended on the sample size; a large rod-like crystal showed a Dysonian ($A / B \sim 2.5$ as shown in Fig. 4), whereas a small needle-like crystal gave a

Lorentzian ($A / B \approx 1.2$).

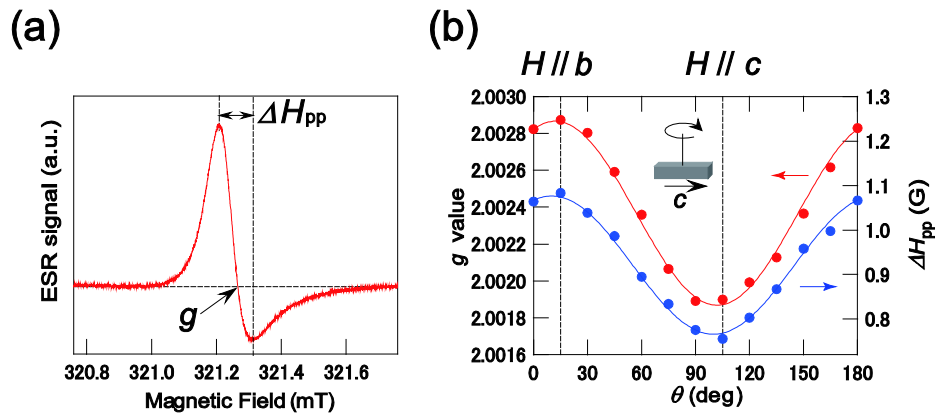


Fig. S8 (a) Definition of the linewidth and the g value in a Dysonian signal. (b) Angle dependence of the g values and the linewidth for the sample rotation around the a axis.

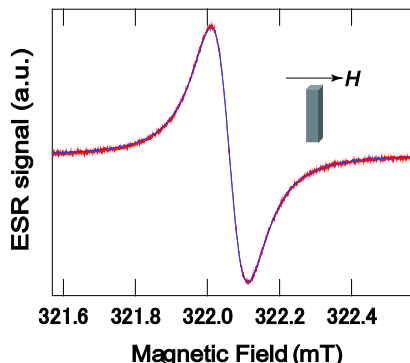


Fig. S9 Lineshape of the ESR signal for $H \perp c$. The blue curve is a fit to the Lorentzian curve.

In order to estimate the critical size, the skin depth is calculated from,^{S6}

$$d = \sqrt{\frac{2}{\mu_0 \sigma \omega}}$$

where d is the skin effect, μ_0 is the magnetic permeability in vacuum, σ is the electrical conductivity, and ω is the frequency of the micro wave. So the skin depth in the a axis is

$$d = \sqrt{\frac{2}{1500 \times 10^2 \text{ S/m} \times 9 \times 10^9 \text{ Hz} \times 4\pi \times 10^{-7} \text{ H/m}}} \\ = 0.3433 \times 10^{-4} \text{ m}$$

$\approx 30 \mu\text{m}$

Then the skin depth in the a axis is estimated to be approximately $30 \mu\text{m}$ from the conductivity ($//c$). The skin depth in the c axis is similarly calculated to be $200 \mu\text{m}$.

The temperature dependence of the ESR intensity (χ) does not basically depend on the field directions and the lineshape. Fig. S10(a) is obtained by using a small needle-like crystal for $H // c$, where the signal is well represented by a Lorentzian. The intensity decreases gradually and finally increases owing to the Curie tail. The linewidth is essentially the same as Fig. 5(b).

Fig. S10(b) presents the ESR results for an Apiezon coated sample for $H \perp c$. The intensity reduces below 110 K, and the linewidth increases at the same time. The drop is slightly shifted to a lower temperature than Fig. 4(a) and (b). This might be ascribed to imperfect suppression of the resistivity jump. Below 100 K both the intensity and the linewidth show a similar behavior to Fig. 5.

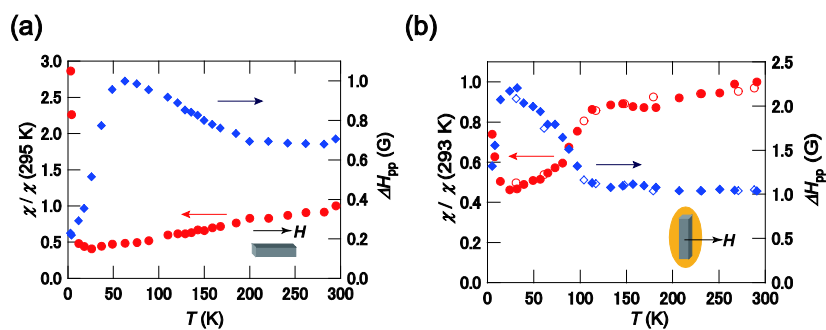


Fig. S10 Temperature dependence of spin susceptibility χ (red circles) and linewidth ΔH_{pp} (blue diamonds) (a) for a nearly Lorentzian signal ($A / B \approx 1.2$ for $H // c$), and (b) for an Apiezon coated sample. The closed and open symbols are for cooling and heating runs, respectively.

References

- (1) H. Meng, L. Zheng, A. J. Lovinger, B.-C Wand, P. G. V.Patten, Z. Bao, *Chem. Mater.*, 2003, **15**, 1778.
- (2) M. C. Burla, R. Caliandro, M. Camalli, B. Carrozzini, G. L. Cascarano, L. de Caro, C. Giacovazzo, G. Polidori, D. Siliqi, R. Spagna, *J. Appl. Crystallogr.*, 2007, **40**, 609.
- (3) G. M. Sheldrick, *Acta Crystallogr., Sect. A* 2008, **64**, 112.
- (4) (a) M. J. S. Dewar, E. G. Zoebisch, E. F. Healy, J. J. P. Stewart, *J. Am. Chem. Soc.*, 1985, **107**, 3902.; (b) T. Mori, A. Kobayashi, Y. Sasaki, H. Kobayashi, G. Saito, H. Inokuchi, *Bull. Chem. Soc. Jpn.*, 1984, **57**, 627.
- (5) T. Mori, K. Imaeda, R. Kato, A. Kobayashi, H. Kobayashi, H. Inokuchi, *J. Phys. Soc. Jpn.*, 1987, **56**, 3429.
- (6) G. Feher, A.F. Kip, *Phys. Rev.*, 1955, **98**, 337.